Article

The International Journal of Robotics Research
2014, Vol. 33(4) 489–506
© The Author(s) 2013
Reprints and permissions:
sagepub.co.uk/journalsPermissions.nav
DOI: 10.1177/0278364913507612
ijr.sagepub.com
SAGE

Design and experimental validation of planar programmable inertia generators

C. Gosselin, A. Lecours, T. Laliberté and M. Fortin

Abstract

This paper investigates the design and experimental development of planar programmable inertia generators. An inertia generator is a hand-held haptic device that has a programmable inertia. By moving internal masses in reaction to accelerations induced by the user, the effective inertia of the device is modified in order to render a prescribed inertia. In this paper, a one-degree-of-freedom device with one internal moving mass is first proposed. The corresponding dynamic model is developed and the rendering capabilities of the device are investigated. Then, a controller is designed to produce the appropriate motion of the internal mass in reaction to the acceleration induced by the user. A prototype is presented and experimental results are discussed. A mechanical architecture is then proposed for the design of a planar three-degree-of-freedom inertia generator. The corresponding dynamic model is derived, and it is shown that the generalized inertia matrix of the proposed mechanism is always of full rank. The rendering capabilities of the device are also investigated. Finally, simulation results obtained with the three-degree-of-freedom inertia generator are reported and discussed.

Keywords

Haptic devices, dynamics, rendering, inertia, hand-held devices

1. Introduction

It is common, for training or entertainment purposes, to actively prescribe the dynamics rendered by a mechatronic device. For instance, impedance control is used in haptics or physical human–robot interaction (pHRI) in order to simulate virtual environments. This approach can be implemented using fixed-base haptic devices which are controlled to produce a desired behavior (see for instance Hannaford and Okamura (2008) and many other references).

In interactive systems (e.g. computer games or training environments), hand-held devices are also often used. These devices are typically passive (Moen, 2007) and are unable to produce kinesthetic feedback. However, as shown in (Laitinen and Maenpaa, 2006; Amemiya et al., 2008; Wever et al., 2013), it is possible to include moving masses in hand-held devices in order to produce the illusion of an external force. This approach can also be used with rotating mechanisms in order to produce the illusion of an external moment (Ando et al., 2004; Nakamura and Fukui, 2006; Winfree et al., 2009).

The work reported in this paper addresses a similar but different challenge. The long-term objective of this initiative is to design a hand-held device that has a programmable inertia. The effective inertia of such a device is modified by moving internal masses in reaction to the accelerations imparted to the hand-held system by the user. Using this approach, the inertia perceived by the user manipulating the hand-held device can be prescribed arbitrarily, within the physical constraints of the mechanical system.

In this paper, a one-degree-of-freedom (1-DOF) inertia generator is first investigated. The main objective of this first phase of the work is to assess the feasibility of the concept. In order to vary the rendered inertia, a moving mass is mounted on a slider within the manipulated 1-DOF physical interface. By moving the internal mass in reaction to an accelerometer signal, a prescribed effective inertia can be rendered. The concept is then extended to a 3-DOF planar inertia generator whose architecture includes four internal moving masses.

The paper is structured as follows: after providing a general description of the concept of inertia generator, the dynamic model of the 1-DOF mechanical system studied here is derived and the limitations on the rendering capabilities of such a device are investigated. Then, a controller

Département de génie mécanique, Université Laval, Canada

Corresponding author:
C. Gosselin, Département de génie mécanique, Université Laval, 1065 Avenue de la Médecine, Québec, QC G1V 0A6, Canada.
Email: gosselin@gmc.ulaval.ca

Downloaded from ijr.sagepub.com at PENNSYLVANIA STATE UNIV on May 10, 2016

is designed to produce the appropriate motion of the internal mass in reaction to the accelerations. A description of the physical 1-DOF prototype is provided and experimental results are discussed. The concept of a 3-DOF inertia generator is then proposed and the corresponding dynamic model is developed. Simulation is used to investigate the rendering capabilities of the device and to provide validation.

2. General concept of inertia generator

The general concept of inertia generator is represented schematically in Figure 1. Consider a box which is held by a user and inside which a set of masses are mounted on actuated sliders or revolute joints. For example, three masses could be mounted on orthogonal actuated rails and three inertias could be mounted on orthogonal actuated pivots. Alternatively, one single rigid body could be attached to the end-effector of a 6-DOF parallel mechanism that can produce translations and rotations of this body in arbitrary directions. When the user imparts accelerations to the box, the latter are measured by a set of accelerometers and the masses are displaced in order to render a prescribed inertia. If the ratio of the moving masses to the mass of the frame of the box is large enough, accelerating the internal masses will produce a significant change in the external apparent inertia of the box. For instance, if the user is accelerating the box along the x-axis and if it is desired to render an inertia that is smaller than the actual inertia of the device, the internal mass(es) will be accelerated in the opposite direction in order to reduce the effective inertia. Similarly, if it is desired to render an inertia that is larger than that of the physical system, then the mass(es) will be moved in the direction of the acceleration imparted by the user in order to increase the apparent inertia.

The principle of the inertia generator is akin to that of motion simulators (Nahon and Reid, 1990) and to that of acceleration compensation for vibration isolation (Graf and Dillmann, 1997; Ebert-Uphoff and Dang, 2004). The performance of such devices is limited by the range of motion of the components—i.e. the range of motion of the internal masses for the inertia generator—and by the limited capabilities of the actuators (maximum velocity and acceleration). Typically, the limitations on the range of motion affect the low-frequency rendering while the limitations on the velocity and acceleration of the actuators affect higher-frequency rendering. In order to alleviate the limiting effect of the range of motion, the concept of a *washout filter* (Hassouneh et al., 2004) used in motion simulators is applied to the inertia generator. The basic principle of a washout filter is to include a low-frequency command in the control loop that aims at bringing the mechanism to a *neutral* configuration so that it is ready for the next acceleration input. The neutral configuration referred to here is defined as one in which all directions of motion are feasible with approximately the same range of motion in all directions. In other words, a washout filter is a high-pass filter aiming at eliminating the very low-frequency content of the input signal which cannot be properly rendered because of limited motion range and which is usually not critical for human perception.

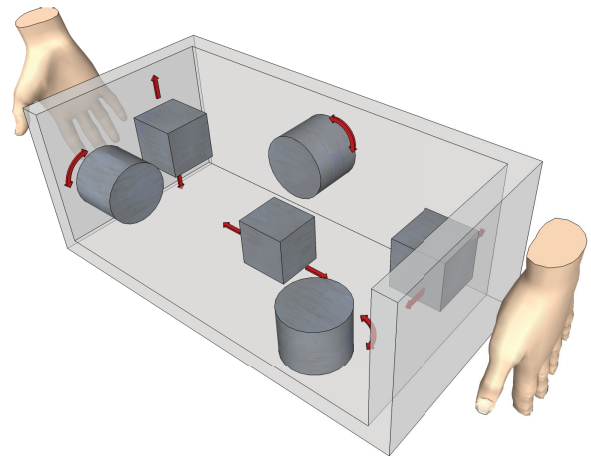

Fig. 1. Schematic representation of the concept of inertia generator.

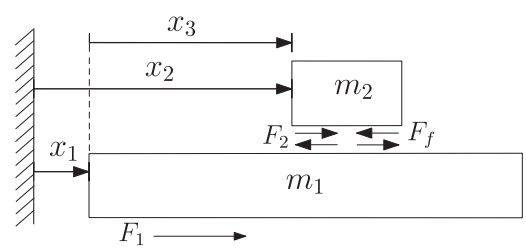

Fig. 2. Schematic representation of the 1-DOF inertia generator.

3. Dynamic modeling of a 1-DOF inertia generator

A schematic representation of a 1-DOF inertia generator is given in Figure 2. The external frame of the device has a mass m_1 and is subjected to the external force F_1 applied by the user. It is assumed that the direction of motion is horizontal. An actuator is included in the device (mounted on the frame) to move a second mass m_2 mounted on a slider attached to the frame of mass m_1. The force applied by the actuator on mass m_2 is noted F_2 while the friction force between the two masses is noted F_f. Relative and absolute coordinates are used in order to ease the derivation of the dynamic model. In this setting, the position of the frame of the device with respect to a fixed inertial frame is noted x_1, the position of mass m_2 with respect to the inertial frame is noted x_2 and x_3 denotes the position of mass m_2 with respect to mass m_1, as shown in Figure 2. Therefore, one has

$$x_2 = x_1 + x_3, \qquad \ddot{x}_2 = \ddot{x}_1 + \ddot{x}_3 \tag{1}$$

As mentioned above, it is desired to render a prescribed inertia, noted m_a, when the user applies forces

Downloaded from ijr.sagepub.com at PENNSYLVANIA STATE UNIV on May 10, 2016

on the device. Therefore, the desired behavior can be expressed as

$$F_1 = m_a \ddot{x}_1 \tag{2}$$

where $\ddot{x}_1$ is the acceleration of mass m_1 with respect to the fixed inertial frame. Applying Newton's second law to each of the moving masses, one obtains

$$F_1 - (F_2 - F_f) = m_1 \ddot{x}_1 \tag{3}$$

$$F_2 - F_f = m_2 \ddot{x}_2 \tag{4}$$

where $\ddot{x}_2$ is the acceleration of mass m_2 with respect to the fixed inertial frame. Substituting equation (1) into equations (3) and (4) and rearranging, one has

$$F_1 = (m_1 + m_2)\ddot{x}_1 + m_2 \ddot{x}_3 \tag{5}$$

$$F_2 = m_2 \ddot{x}_1 + m_2 \ddot{x}_3 + F_f \tag{6}$$

Equations (5) and (6) represent the dynamics of the 2-DOF system comprising the mobile frame of mass m_1 and the sliding mass m_2. Referring to equation (2), it is desired to obtain an expression for the force F_2 to be applied by the actuator in order to render the prescribed inertia m_a. To this end, equation (2) is first substituted into equation (5), which leads to

$$m_2 \ddot{x}_3 = (m_a - m_1 - m_2)\ddot{x}_1 \tag{7}$$

Substituting the latter equation into equation (6) then leads to

$$F_2 = (m_a - m_1)\ddot{x}_1 + F_f \tag{8}$$

Finally, equation (7) is rearranged in order to determine the acceleration required at the actuator, namely by rewriting it as

$$\ddot{x}_{d3} = \frac{(m_a - m_1 - m_2)\ddot{x}_1}{m_2} \tag{9}$$

where $\ddot{x}_{d3}$ is the desired relative acceleration.

4. Rendering capabilities of the 1-DOF inertia generator

For a given frame mass m_1 and internal mass m_2, the rendering capabilities of an inertia generator are limited by two main design parameters, namely, the motion range of the internal moving mass and the velocity and acceleration limitations of the actuator. The effect of these two constraints are now investigated.

4.1. Limitations on the motion range of the moving mass

In a practical situation, an inertia generator is likely used in the vicinity of a given reference position around which it is moved by a user. Although the motions imparted by the user are somewhat arbitrary, they can always be represented as a sum of harmonic functions, using a Fourier series for instance. Therefore, in order to analyze the rendering capabilities of such a device, a harmonic input function (user imparted motion) is assumed. One writes, using the notation of the preceding section

$$x_1 = r \sin \omega t, \qquad \dot{x}_1 = r\omega \cos \omega t, \qquad \ddot{x}_1 = -r\omega^2 \sin \omega t \tag{10}$$

where t is the time and where ω and r are respectively the frequency and the amplitude of the input motion. Substituting the above expression for $\ddot{x}_1$ into equation (7), one then obtains

$$\ddot{x}_3 = \frac{-(m_a - m_1 - m_2) r\omega^2 \sin \omega t}{m_2} \tag{11}$$

Assuming a steady state sinusoidal trajectory, the motion of mass m_2 relative to mass m_1 that renders the prescribed inertia m_a can therefore be written as:

$$x_3 = \frac{(m_a - m_1 - m_2) r \sin \omega t}{m_2}. \tag{12}$$

The latter trajectory is feasible as long as the motion range of mass m_2 is larger than the amplitude of the above sine function. Assuming a range of motion for m_2 of $2a$, i.e.

$$-a \le x_3 \le a \tag{13}$$

and by considering the bounds on the sine function, one then obtains, by substituting equation (12) into equation (13),

$$-a \le \left(\frac{(m_a - m_1 - m_2) r}{m_2} \right) \le a. \tag{14}$$

The minimum and maximum prescribed inertia that can be rendered, for a given input motion range, r, and a given motion range of the moving mass, a, can then be obtained by rearranging equation (14) as

$$\left(m_1 + m_2 - \frac{m_2 a}{r} \right) \le m_a \le \left(m_1 + m_2 + \frac{m_2 a}{r} \right) \tag{15}$$

The above inequalities are represented graphically in Figure 3 where $M = m_1 + m_2$ is the total mass of the device and where the shaded area represents the range of prescribed inertia (more precisely the ratio of the prescribed inertia to the total mass) that can be rendered for a given ratio of the input motion range to the motion range of the moving mass. This graph can be used as a guideline in order to establish the capabilities of a device at the design stage. The horizontal asymptote on the graph represents a prescribed inertia equal to the total moving mass, which can always be rendered since it does not require any motion of mass m_2. The two curves are symmetric with respect to this asymptote since the motion of mass m_2 can be inverted depending on whether the prescribed inertia is larger or smaller than the actual total mass. It can also be observed that a zero virtual mass can theoretically be rendered as long

Downloaded from ijr.sagepub.com at PENNSYLVANIA STATE UNIV on May 10, 2016

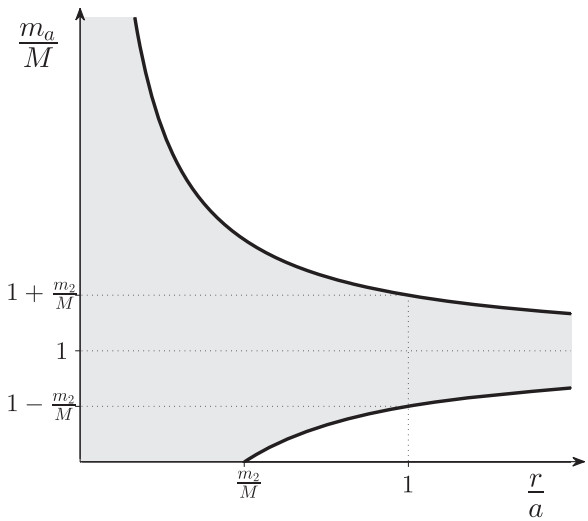

Fig. 3. Ratio of the prescribed inertia that can be rendered by the inertia generator to the total actual mass as a function of the ratio of the input motion range to the motion range of the moving mass. The shaded area represents the feasible region.

as the ratio of the input motion range to the range of motion of m_2 is smaller than or equal to the ratio of mass m_2 to the total moving mass. Increasing the latter ratio therefore improves the performances of the device. In all cases, the maximum motion ratio (input range to actuation range) for which a zero virtual inertia can theoretically be rendered is always smaller than one. Also, when the input motion range to actuation range is equal to one, the feasible range of rendered mass to total mass ratio is bounded by $1-(m_2/M)$ and $1+(m_2/M)$, which further emphasizes the importance of maximizing the moving mass to total mass ratio, m_2/M. Finally, it can be observed that the rendering capabilities represented by the graph of Figure 3 are independent from the frequency of the input motion. The only quantities that are relevant in the assessment of the rendering capabilities based on the limitations on the motion range of mass m_2 are thus the ratio of the masses (moving mass to total mass) and the ratio of the input motion range to the moving mass motion range. The limitations related to the frequency of the input motion are studied in the next subsection.

4.2. Limitations on the velocity and acceleration of the actuator

4.2.1. Acceleration limits Referring to equation (11), it is apparent that the magnitude of the acceleration required at the actuator in order to render a prescribed inertia m_a is proportional to the square of the input frequency. Therefore, limitations on the acceleration capabilities of the actuator limit the frequency of the input motion for which a prescribed mass can be rendered. It should also be pointed out that the force (or acceleration) limitations of the actuator correspond to limitations on F_2—or equivalently on $\ddot{x}_2$—since the force transmitted to the moving mass m_2 is entirely provided by the actuator. Hence, substituting equation (10) into equation (8) and neglecting friction, one obtains

$$\omega^2 = \frac{F_{2a}}{r|m_a - m_1|} \tag{16}$$

where F_{2a} is the actuator force corresponding to a prescribed inertia m_a. If the actuator force F_2 is limited to $F_{2,\max}$, the maximum frequency for which a prescribed inertia m_a can be correctly rendered is therefore given by

$$\omega_{\max}^2 = \frac{F_{2,\max}}{r|m_a - m_1|} \tag{17}$$

Above this frequency, the rendered inertia, noted m_r, differs from the prescribed inertia m_a. Dividing equation (16) by equation (17), one then obtains

$$\frac{F_{2a}}{F_{2,\max}} = \frac{\omega^2}{\omega_{\max}^2} \tag{18}$$

In order to assess the performance of the inertia generator, the ratio between m_r and m_a is now determined for frequencies above $\omega_{\max}$. Consider a situation in which $\omega > \omega_{\max}$ and for which it is desired to render a prescribed inertia m_a. In this situation, the force required at the actuator in order to render the inertia m_a, F_{2a}, exceeds the capabilities of the actuator, i.e. $F_{2a} > F_{2,\max}$. Referring to equation (8), one can write

$$F_{2a} = (m_a - m_1)\ddot{x}_1 \tag{19}$$

However, since the actuator cannot produce a force of magnitude F_{2a}, it is limited to $F_{2,\max}$ and the rendered inertia, noted m_r, rather corresponds to

$$F_{2,\max} = (m_r - m_1)\ddot{x}_1 \tag{20}$$

Dividing equation (20) by equation (19) and recalling equation (18), one then obtains

$$\frac{m_r - m_1}{m_a - m_1} = \frac{F_{2,\max}}{F_{2a}} = \frac{\omega_{\max}^2}{\omega^2} \tag{21}$$

which can be rearranged as

$$\frac{m_r}{m_a} = \frac{m_1}{m_a} + \left(1 - \frac{m_1}{m_a}\right)\frac{\omega_{\max}^2}{\omega^2} \tag{22}$$

The latter expression represents the ratio of the rendered inertia m_r over the prescribed inertia m_a for input frequencies that are above the maximum input frequency for which m_a can be rendered. This is illustrated in Figure 4 where it can be observed that up to an input frequency $\omega_{\max}$, given by equation (17), the prescribed inertia m_a can be rendered while above this frequency, the rendered inertia m_r differs from m_a. For very high frequencies, the rendered inertia converges to m_1, since force F_2 becomes negligible compared to F_1, and hence the rendered inertia is only due to m_1.

The effect of the force limitation on the acceleration profile of mass m_2 is represented schematically in Figure 5. It is pointed out that the rendered inertia predicted by equation (22) corresponds to the worst case over a complete input cycle and that it occurs at only two points of the trajectory. Therefore, this assessment is rather conservative.

Downloaded from ijr.sagepub.com at PENNSYLVANIA STATE UNIV on May 10, 2016

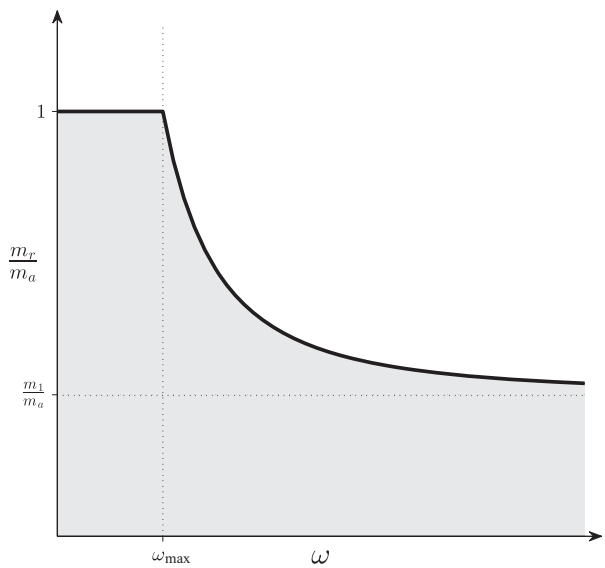

Fig. 4. Ratio of the rendered inertia over the prescribed inertia as a function of the frequency of the input motion considering the acceleration limit of the actuator.

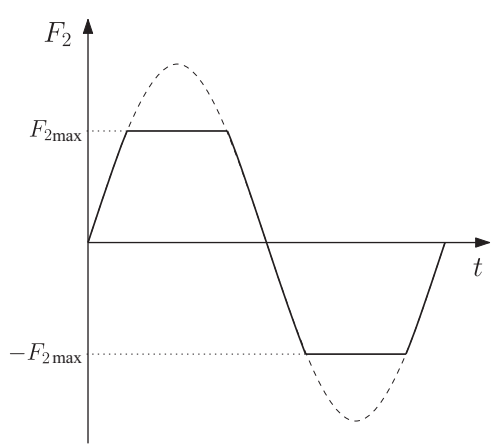

Fig. 5. Illustration of the effect of the force (acceleration) limitation.

4.2.2. Velocity limits The derivation of the previous subsection assumes that acceleration is the limiting factor on the actuator motion. However, it should also be verified that the velocities required in order to produce the actuator motion do not exceed the capabilities of the actuator. The limitations introduced by the maximum velocity of the actuator are associated with variable $\dot{x}_3$—whereas the acceleration limits are associated with variable $\ddot{x}_2$—since $\dot{x}_3$ represents the relative velocity between masses m_1 and m_2. From equation (7) and assuming the steady-state harmonic input motion of equation (10), one can write

$$m_2\dot{x}_3 = (m_a - m_1 - m_2)\dot{x}_1 \tag{23}$$

Using equation (10), the latter equation can also be written as

$$\omega = \frac{m_2\dot{x}_{3,a}}{r|m_a - m_1 - m_2|} \tag{24}$$

where $\dot{x}_{3,a}$ stands for the actuator velocity that is required in order to render a prescribed inertia m_a.

The maximum velocity that can be produced by the actuator is noted $\dot{x}_{3,\max}$. Hence, the maximum input frequency for which a prescribed inertia m_a can be rendered without exceeding the velocity limit of the actuator is obtained by substituting equation (10) into equation (23), leading to

$$\omega'_{\max} = \frac{m_2\dot{x}_{3,\max}}{r|m_a - m_1 - m_2|} \tag{25}$$

where the maximum frequency associated with the velocity limitation is noted $\omega'_{\max}$ in order to distinguish it from the maximum frequency associated with the accleration limitation. Dividing equation (25) by equation (24), one then obtains

$$\frac{\omega'_{\max}}{\omega} = \frac{\dot{x}_{3,\max}}{\dot{x}_{3,a}} \tag{26}$$

Similarly to what was done in the previous subsection, a situation for which $\omega > \omega'_{\max}$ is now considered. The situation resulting from a required velocity $\dot{x}_{3,a}$ that exceeds the capabilities of the actuator is depicted schematically in Figure 6. The impact on the rendering is different from that of the acceleration limitation. Indeed, the velocity limit produces a portion of the trajectory for which the velocity is constant, and hence the acceleration $\ddot{x}_3$ is equal to zero on this portion of the trajectory. Therefore, referring to equation (5) or equation (7), it is apparent that the rendered inertia is equal to $(m_1 + m_2)$ for that portion of the input trajectory. Hence, the worst case rendering over an input cycle corresponds to $m_r = (m_1 + m_2)$, which corresponds to the portion of the trajectory in which the acceleration of m_2 with respect to m_1 is equal to zero. This result is represented in Figure 7. Similarly to the case of the acceleration limit, this assessment is rather conservative, especially because the velocity limit affects the portion of the trajectory in which the acceleration is small. Therefore, the impact on the perceived inertia may not be as drastic as represented in Figure 7.

4.2.3. Combined limits In a practical design or control situation, the most limiting condition (velocity or acceleration) determines the actual performance of the mechanism. Whether the velocity or the acceleration is the most limiting factor depends on the physical limits of the actuator ($F_{2,\max}$ and $\dot{x}_{3,\max}$), the input motion amplitude (r), the device's masses (m_1 and m_2) and the prescribed inertia (m_a). An example situation (corresponding to the prototype used in this work) is depicted in Figure 8 where the range of frequencies that can be rendered for a given input motion to motion range ratio (r/a) is plotted as a function of the ratio of the prescribed inertia m_a to the total mass of the device

Downloaded from ijr.sagepub.com at PENNSYLVANIA STATE UNIV on May 10, 2016

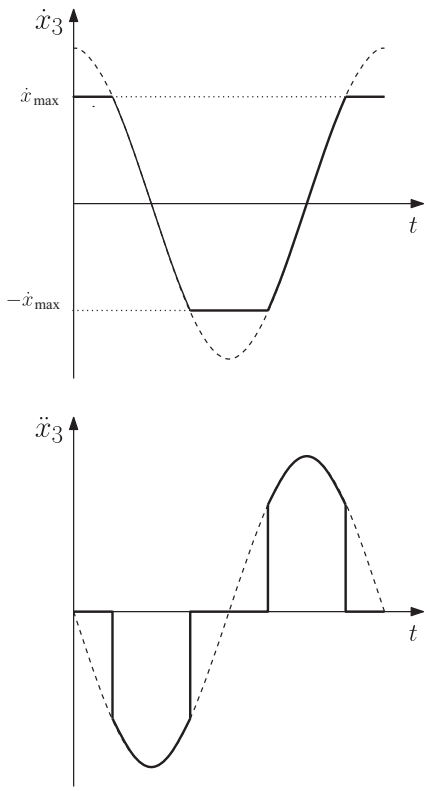

Fig. 6. Illustration of the effect of the velocity limitation.

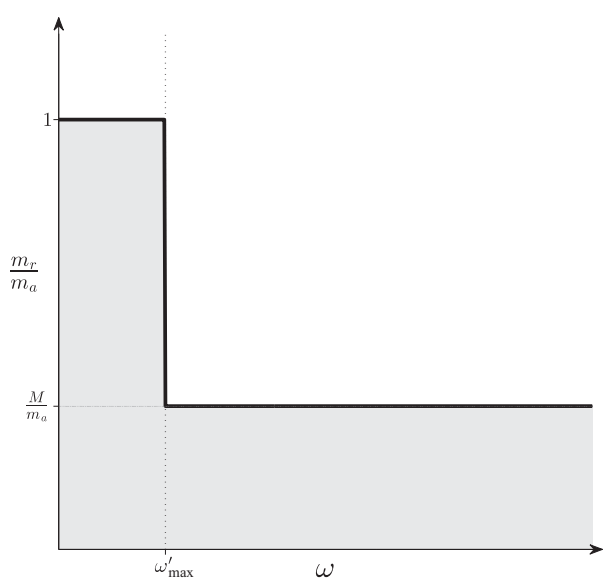

Fig. 7. Ratio of the rendered inertia over the prescribed inertia as a function of the frequency of the input motion considering the velocity limit of the actuator.

$(m_1 + m_2)$. The shaded area represents the range of frequencies for which the prescribed inertia can theoretically be rendered. It can be observed that, depending on the prescribed inertia, the limitation on the frequency may be due to the velocity or acceleration limit of the actuator. It should

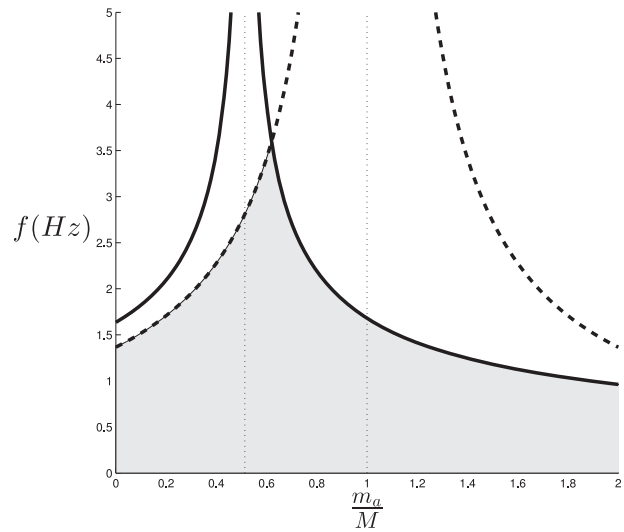

Fig. 8. Range of frequencies of the input motion for which the prescribed inertia can be rendered considering the velocity and acceleration limits of the actuator ($\dot{x}_{3,\max} = 1.5$ m/s, $F_{2,\max} = 22$ N, $m_1 = 2.45$ kg, $m_2 = 2.32$ kg), for an input motion amplitude to range ratio of $(r/a) = 0.5$. The shaded area represents the feasible range of frequencies. The solid lines represent the boundaries due to acceleration limits while the dashed lines represent boundaries due to velocity limits.

also be pointed out that the curves shown in Figure 8 are also dependent on the mass ratio, m_2/M.

5. Controller Design

Based on the dynamic model presented in Section 3, a control scheme is developed in order to render the prescribed inertia m_a. The controller is designed to react to the acceleration of the moving frame of mass m_1. To this end, an accelerometer is mounted on the frame, which provides a measurement of its acceleration $\ddot{x}_1$. The control strategy is based on the combination of three terms, namely: a feedforward term (including friction compensation), a feedback term, and a washout term. Each of these contributions is now detailed.

5.1. Feedforward and friction compensation

The feedforward term is based on the dynamic model developed in Section 3. Equation (8) is used to compute an estimation of the force to be applied by the actuator based on the measured acceleration $\ddot{x}_1$ and on an estimation of the friction force F_f. A simple friction compensation can be written as:

$$F_f = f_c + f_v \tag{27}$$

where f_c and f_v are respectively the Coulomb and viscous friction forces with

$$f_c = c(1 - e^{-\alpha|\dot{x}_{d3}|})\, sign(\dot{x}_{d3}) \tag{28}$$

$$f_v = v\dot{x}_{d3} \tag{29}$$

Downloaded from ijr.sagepub.com at PENNSYLVANIA STATE UNIV on May 10, 2016

where c is the Coulomb friction coefficient, v the viscous friction coefficient and α is a tuning parameter. The exponential term is used to reduce the chattering induced by friction compensation when the velocity is near zero. The desired velocity, $\dot{x}_{d3}$, is used for friction compensation in order to reduce the command noise, although the measured velocity could also be used. Other more complex friction models could also be used (see for instance Armstrong-Helouvry et al. (1994)), including stiction for example, but the simple friction compensation given in equation (27) provides good experimental results, as will be shown in the next section.

5.2. Feedback

The desired acceleration of mass m_2 can be computed using equation (9). In order to achieve this relative acceleration, it would be possible to use a feedback control (e.g. PID control) with a relative acceleration measurement (e.g. accelerometer or second derivative of the position). However, acceleration control is not very practical, mainly because the measured acceleration is known to be very noisy. Instead, velocity or position control is implemented using an integration technique.

First, the discrete desired velocity required to render the desired acceleration is obtained with a zero-order-hold integration (alternatively, a bilinear discretization can be used):

$$\dot{x}_{d3}(k) = \dot{x}_{d3}(k-1) + \ddot{x}_{d3}(k)\,T_s \tag{30}$$

while the position is obtained by integrating a second time, namely:

$$x_{d3}(k) = x_{d3}(k-1) + \dot{x}_{d3}(k-1)\,T_s + \frac{1}{2}\ddot{x}_{d3}(k)\,T_s^2 \tag{31}$$

where T_s is the sampling period, k is the time step and x_{d3}, $\dot{x}_{d3}$, and $\ddot{x}_{d3}$ are respectively the desired position, velocity and acceleration.

One should note that this integration method is used to achieve acceleration control in pHRI with admittance control schemes (Lecours et al., 2012) and that, although it is preferable to use the desired velocity of the preceding step ($\dot{x}_{d3}(k-1)$), the measured velocity can alternatively be used in the above equations. The desired acceleration is then rendered using velocity or position control, which is more practical and can be achieved using a simple PID controller or more advanced algorithms.

5.3. Washout

As explained in Section 2, the goal of the washout filter is to ensure that the moving mass is kept as close as possible to its neutral position in order to be ready to accommodate arbitrary acceleration inputs. For the 1-DOF system studied here, this amounts to keeping mass m_2 as close as possible to its mid-range position in order to avoid the mechanical limits (end of stroke). To this end, a virtual spring-damper system modelled as follows is used:

$$F_w = -K_w(x_3 - x_w) - C_w\dot{x}_3 \tag{32}$$

where F_w stands for the washout force, K_w is the washout spring stiffness, C_w is the washout damping factor and x_w is the neutral position. The adjustment of the washout parameters is based on the analysis of the above second-order system. Knowing the mass to be moved m_2, one obtains

$$K_w = m_2\omega_w^2 \tag{33}$$

$$C_w = 2m_2\zeta_w\omega_w \tag{34}$$

where ω_w is the washout frequency and ζ_w is the damping factor. The washout frequency should be chosen low enough so that it does not significantly impact the rendering. On the other hand, it should be high enough to ensure that mass m_2 is kept sufficiently close to its neutral position. In order to cope with this compromise, the washout frequency is adjusted according to the acceleration of the frame, $\ddot{x}_1$. The following heuristic rule is used:

$$\omega_w = \begin{cases} 0 & \text{if } |\ddot{x}_1| > \ddot{x}_{1t} \\ \omega_{w0}\left(1 - \frac{\ddot{x}_1^2}{\ddot{x}_{1t}^2}\right) & \text{otherwise} \end{cases} \tag{35}$$

where ω_{w0} is the default washout frequency and $\ddot{x}_{1t}$ is an acceleration threshold above which the washout is deactivated. In this work, $\omega_{w0} = 2\ \mathrm{s}^{-1}$ and $\ddot{x}_{1t} = 0.3\ \mathrm{ms}^{-2}$ are used for the 1-DOF prototype.

5.4. Internal motion limits

The motion of the internal mass m_2 is limited by the stroke allowed by the slider on which it is mounted. Therefore, limitations must be imposed on $\ddot{x}_{d3}$, $\dot{x}_{d3}$ and x_{d3} in order to account for these physical limits and avoid collisions with the end stops. To this end, saturation limits are imposed on the desired position, velocity and acceleration calculated from equations (9), (30) and (31). It is pointed out that, although the limitation is primarily on the position x_{d3}, the velocity and acceleration $\dot{x}_{d3}$ and $\ddot{x}_{d3}$ must also be recomputed based on this limitation. Moreover, the limitation should also be taken into account in the feedforward term. To this end, the value of $\ddot{x}_{d3}$ obtained after saturation is injected in equation (6).

6. Experiments

The prototype used in the experiments reported in this paper is shown in Figure 9. Mass m_1 consists of an aluminium plate equipped with wheels that can roll with low friction on a table top or on a floor. A DC motor is mounted on the plate together with a rail and pulleys while mass m_2 consists of a small steel plate and a trolley. The motion of mass m_2 is actuated by the DC motor which is connected to the mass via a closed-loop belt. An accelerometer is

Downloaded from ijr.sagepub.com at PENNSYLVANIA STATE UNIV on May 10, 2016

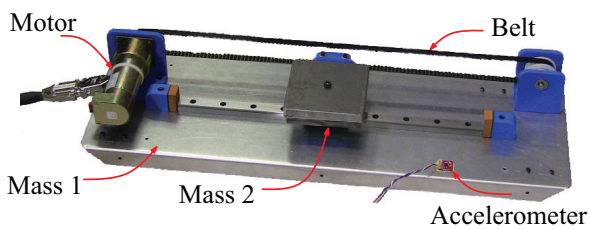

Fig. 9. Prototype of a 1-DOF inertia generator used in the experiments.

mounted on the base plate in order to measure the acceleration of the frame, $\ddot{x}_1$. Also, an ATI MINI-40 force/torque sensor can be attached to the plate to measure the force F_1 applied by the user on the inertia generator and a second accelerometer can be mounted on mass m_2. The latter two measurements (force F_1 and acceleration $\ddot{x}_2$) are not used by the controller but only for experimental validation and analysis. Therefore, they are not shown in Figure 9.

6.1. Model validation

A first experiment is performed in order to validate the dynamic model. In this experiment, the frame (mass m_1) is moved manually while the second mass (m_2) is free to slide on the rail. The interaction force (F_1) and the acceleration of each of the masses ($\ddot{x}_1$ and $\ddot{x}_2$) are measured. The measured accelerations are then compared with those computed using the measured force and the dynamic equations, in order to validate the model. The results are shown in Figure 10. It can be observed that, although the results are not perfect, the model is sufficiently realistic to be used for control purposes.

6.2. Interaction experiments

Experiments are then performed using the prototype described above, which has the following characteristics: $m_1 = 2.45$ kg and $m_2 = 2.32$ kg, for a total moving mass of 4.77 kg. It can be observed experimentally (qualitatively) that variations of the prescribed inertia m_a are easily perceived by the user. To obtain quantitative observations, the force and acceleration are recorded in order to compare the results with the desired dynamics given by equation (2). Considering the characteristics of the prototype (the masses given above and the range of motion of mass m_2, namely $a = 0.17$ m) and an approximate input range of motion observed in the experiments, equation (15) can be used to estimate the rendering capabilities, which leads to

$$\sim 1\text{kg} \leq m_a \leq \sim 8.5\text{kg}. \tag{36}$$

Hence, prescribed inertias within this range are used in the experiments.

Figure 11 presents the results obtained with a prescribed mass varying from $m_a = 1.25$ kg to $m_a = 6.00$ kg. The graphs provide a comparison of the force applied by the user

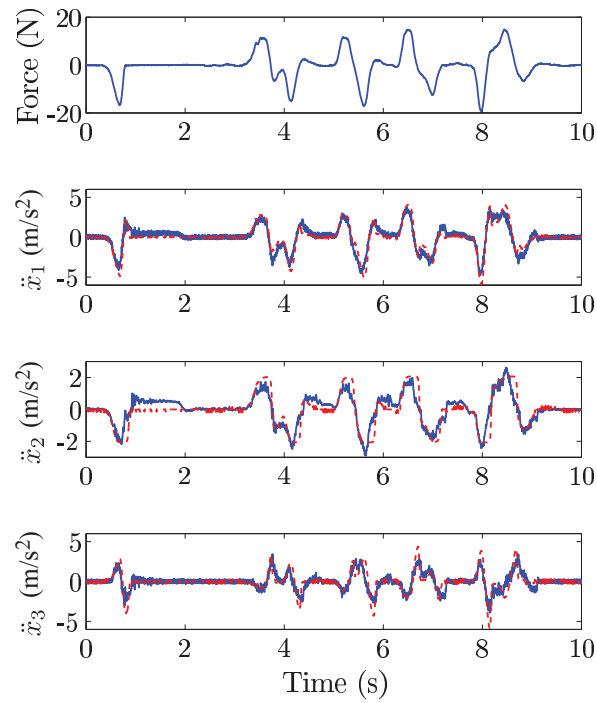

Fig. 10. Model validation. The solid lines represent measured quantities while the dashed lines represent accelerations computed using the dynamic model and the measured force.

(measured) and the rendered force ($m_a\ddot{x}_1$) where $\ddot{x}_1$ is the measured acceleration. A video demonstrating the operation of the 1-DOF inertia generator is available in Extension 1 of this paper.

7. Discussion

It can be observed from the experimental results that the prescribed inertia is generally well rendered. When the prescribed inertia is close to the total mass ($m_1 + m_2$), e.g. with $m_a = 4.77$ kg, the results are obviously very good since the demands on the actuator velocity are very low. These results can serve as a base line for the analysis of the results obtained in more demanding situations. Basically, if m_a is close to ($m_1 + m_2$), the errors correspond to the estimation errors introduced by the control loop and the measurements themselves. Similarly, when the prescribed inertia is close to the mass of the frame m_1, e.g. with $m_a = 2.45$ kg, the results are also very good because the force demands on the actuator are very low. Indeed, in this case mass m_2 is almost not moving with respect to the inertial frame, and hence the actuator torque is very low.

When the prescribed inertia is more significantly different from the total mass, the actuator is much more sollicited and the error tends to increase, as observed in Figures 11(a) and 11(d). Nevertheless, the results are still acceptable, especially considering that the perceptual resolution capabilities of the user are limited. For example, with $m_a = 1.25$ kg (Figure 11(a)) the rendered mass is approximately 1.5

Downloaded from ijr.sagepub.com at PENNSYLVANIA STATE UNIV on May 10, 2016

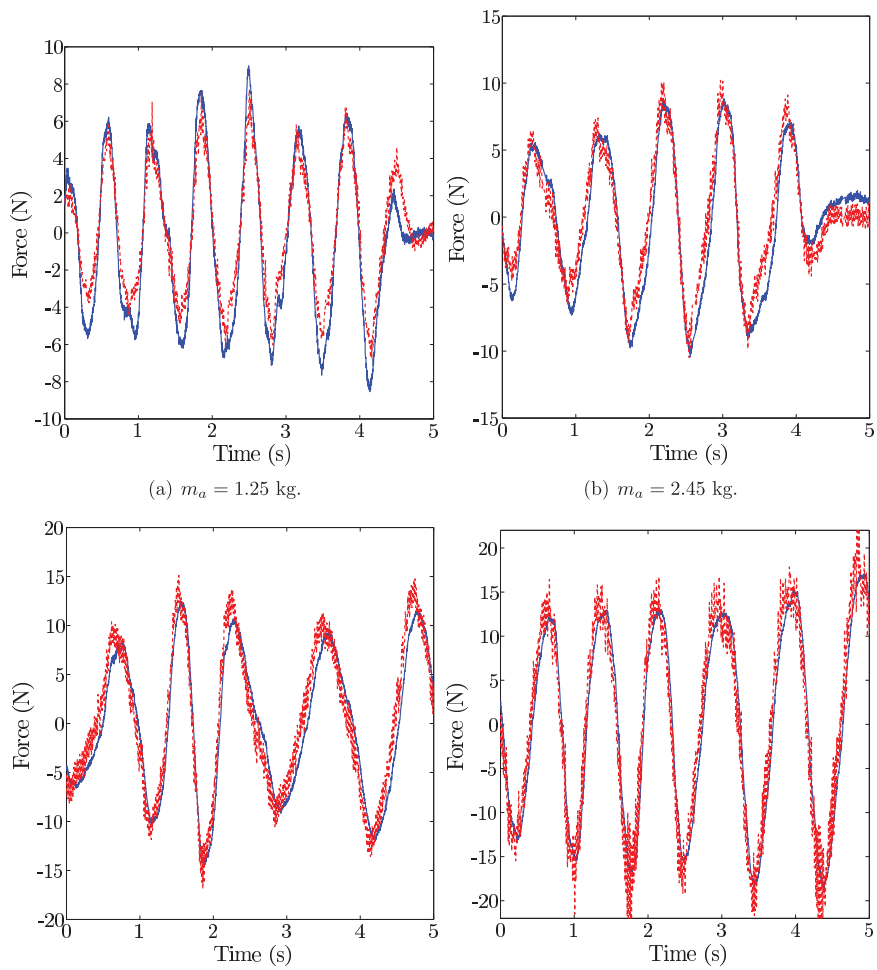

(a) $m_a = 1.25$ kg. (b) $m_a = 2.45$ kg.

(c) $m_a = 4.77$ kg. (d) $m_a = 6.00$ kg.

Fig. 11. Experimental results obtained with the prototype for different values of the prescribed inertia m_a. The solid lines represent the measured force while the dashed lines represent the model force ($m_a\ddot{x}_1$) where $\ddot{x}_1$ is measured with an accelerometer.

kg. It can be observed in the latter figure that the measured forces are slightly larger than the prescribed forces. On the other hand, if the prescribed inertia is larger than the total mass, e.g. $m_a = 6.00$ kg (Figure 11(d)), the measured forces tend to be slightly smaller than the prescribed forces. These results demonstrate the feasibility of the concept and they confirm the applicability of the design guidelines provided in Section 4. They also highlight the importance of properly selecting the ratio between m_2 and m_1, which in turn raises the issue of the power to mass ratio of the actuator. Ideally, the mass ratio (m_2/m_1) should be maximized so that the impact of the moving mass is maximized, as shown in Figure 3. One possible design avenue is then to include the actuator in the moving mass in order to increase the mass ratio. Using this principle, the power to mass ratio of the actuator becomes less important.

The experimental results reported in Section 6 can also be analyzed based on the rendering capabilities discussed in Section 4. First, the time plots of Figure 11 are subjected to a frequency analysis in order to extract the dominant input frequency and its associated motion amplitude, r. The limitations of the prototype are then considered, namely $F_{2,\max} \simeq 22$ N, $\dot{x}_{3,\max} \simeq 1.5$ m/s. Based on these characteristics, equations (17) and (25) are used to determine the range of input frequencies for which a given prescribed inertia can be rendered, which is compared with the dominant input frequency extracted from the experimental data. Figure 12 shows the feasible frequency range as a function of the input motion amplitude considering the velocity and acceleration limitations of the prototype for different values of the prescribed inertia. Depending on the situation, the frequency range is limited either by the velocity or the acceleration constraint. For example, when the prescribed inertia is low (for instance with $m_a = 1.25$ kg, Figure 12(a)), acceleration is the main limiting factor for small input motion ranges while velocity is the limiting factor for larger input motion amplitudes. When the prescribed mass is equal to the mass of the frame m_1, ($m_a = 2.45$ kg, Figure 12(b)), the actuator is theoretically not applying any force, which means that the force constraint is not active. The frequency limitation is therefore solely due to the velocity constraint, as shown on the graph. In this

Downloaded from ijr.sagepub.com at PENNSYLVANIA STATE UNIV on May 10, 2016

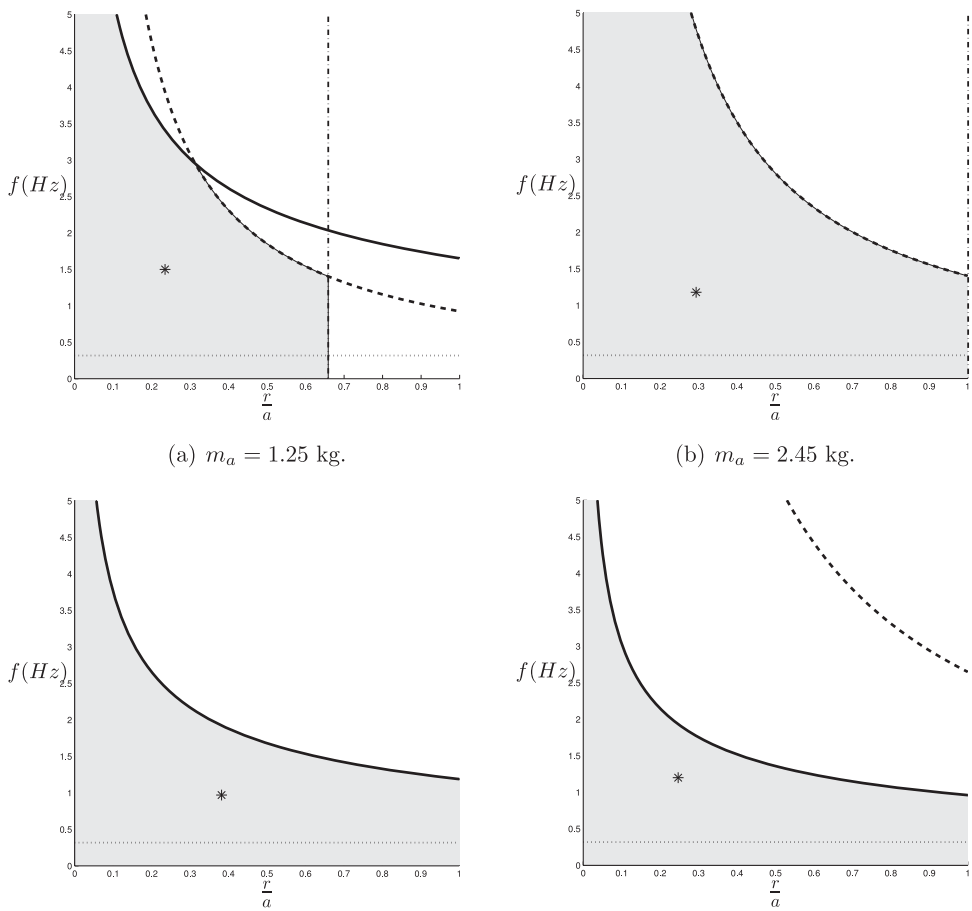

(a) $m_a = 1.25$ kg. (b) $m_a = 2.45$ kg.

(c) $m_a = 4.77$ kg. (d) $m_a = 6.00$ kg.

Fig. 12. Feasible frequency range as a function of the input motion amplitude considering the position, velocity and acceleration limitations of the prototype for different values of the prescribed inertia. The solid lines represent the acceleration limitations while the dashed lines represent the velocity limitations. The dashed-dotted vertical lines represent the limitations due to the range of motion while the dotted horizontal lines represent the washout filter frequency. The shaded area represents the feasible range, knowing that the performances may deteriorate when operating close to or below the washout filter frequency. The stars indicate the frequency and the input motion range of the dominant input motion for each of the experiments (point of operation) with (a) $m_a = 1.25$ kg, (b) $m_a = 2.45$ kg, (c) $m_a = 4.77$ kg and (d) $m_a = 6.00$ kg.

situation, although the actuator does not apply any force, it must move fast enough to produce the relative motion required between the two masses. On the other hand, when the prescribed mass is equal to the total mass of the device ($m_a = 4,77$ kg, Figure 12(c)), the actuator is theoretically not moving, which means that the velocity constraint is not active. The frequency limitation is therefore solely due to the acceleration constraint. Indeed, although the actuator is not moving, it still has to produce the torque required to accelerate mass m_2 with respect to the inertial frame. Finally, when the prescribed mass is large (for instance with $m_a = 6,00$ kg, Figure 12(d)), the main constraining factor is the acceleration, although the velocity limitation reappears on the graph.

The limitations due to the finite range of motion, a, of mass m_2 can also be assessed. First, equation (15) is used to determine the maximum input motion range for which the prescribed mass m_a can be rendered. Based on the physical parameters of the prototype, the maximum value of the input to range ratio can be calculated for each of the situations depicted in Figure 12, yielding $(\frac{r}{a})_{\max} = 0.659$ for $m_a = 1.25$ kg, $(\frac{r}{a})_{\max} = 1$ for $m_a = 2.45$ kg, $(\frac{r}{a})_{\max} \to \infty$ for $m_a = 4.77$ kg, and $(\frac{r}{a})_{\max} = 1.886$ for $m_a = 6$ kg. The corresponding limits (vertical dashed-dotted lines) are shown in Figure 12(a) and (b) while they are outside of the plotting limits for the other two cases. The limited motion range of mass m_2 is also reflected by the use of a washout filter, which affects the rendering performance. Although it is not easy to represent precisely the effect of the washout filter on the graphs of Figure 12, the following reasoning can be used. Referring to equation (35), it is recalled that the washout filter is progressively activated when the input

Downloaded from ijr.sagepub.com at PENNSYLVANIA STATE UNIV on May 10, 2016

acceleration $\ddot{x}_1$ is lower than a prescribed threshold $\ddot{x}_{1t}$. For a periodic input motion, there are always points of the trajectory for which the acceleration is zero, i.e. points for which the washout filter is operating at its maximum frequency. Therefore, it can be expected that when the input motion is taking place at a frequency close to or lower than the maximum frequency of the washout filter, ω_{w0}, the rendering is likely to be affected. The maximum frequency of the washout filter used in the experiment is equal to approximately 0.32 Hz and is represented as a horizontal dotted line on the graphs of Figure 12. When operating in the areas located below this line, a deterioration of the rendering performances is likely to occur.

Finally, the stars appearing on each of the four graphs indicate the point of operation of each of the experiments reported in Figure 11, i.e. the dominant frequency appearing in the input motion and the corresponding input motion amplitude. It can be observed that, in each case, the point of operation is within the feasible frequency range, which explains the good rendering results. It can also be observed that for the more demanding cases, e.g. with $m_a = 6.00$ kg, shown in Figure 12(d), the point of operation is closer to the boundary, thereby leading to a slight performance degradation.

8. Planar 3-DOF inertia generator

A planar 3-DOF inertia generator is now considered. This mechanism aims at rendering inertias in the plane, including rotational inertia around an axis orthogonal to the plane. In a practical implementation, the generator will be mounted on omnidirectional wheels, spherical wheels, low friction pads or an air table.

8.1. Dynamic modeling

The planar 3-DOF inertia generator proposed here consists of a square frame with rails mounted on its edges, as shown in Figure 13. A moving mass m_i, $i = 1, \ldots, 4$, is mounted on the ith rail and its displacement along the rail is controlled by an actuator. Therefore, there are four actuators in the mechanism. A fixed inertial reference frame Oxy is defined on the ground, while a moving frame Cx_0y_0 is attached to the inertia generator, with its origin at the centroid of the square frame. The position vector of the centroid of the square frame with respect to the origin of the fixed reference frame is noted $\mathbf{c}_0$ while the position vector of the center of mass of mass m_i with respect to the origin of the fixed frame is noted $\mathbf{c}_i$. The rotational inertia of mass m_i is noted I_i, the unit vector along the ith slider is noted $\mathbf{e}_i$ and the position coordinate of mass m_i along the slider is given by s_i, measured from the mid-point of the motion range. The vector connecting the centroid of the square frame and the mid-point of the slider on which mass m_i is mounted is noted $\mathbf{c}_{i0}$. Finally, the orientation of the moving frame with respect to the fixed frame is given by the angle between

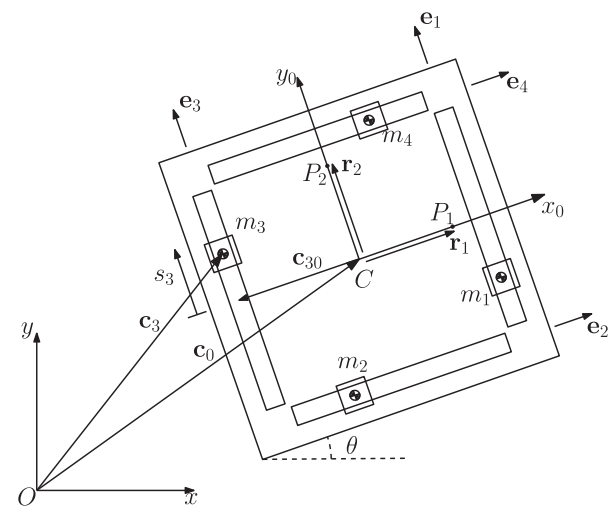

Fig. 13. Kinematic modeling of the planar 3-DOF inertia generator.

the x-axis of the fixed frame and the x_0-axis of the moving frame, noted θ. One can then write the position vector of the center of mass of mass m_i with respect to the origin of the fixed frame as

$$\mathbf{c}_i = \mathbf{c}_0 + \mathbf{c}_{i0} + s_i\mathbf{e}_i, \quad i = 1, \ldots, 4 \tag{37}$$

Differentiating twice with respect to time, one then obtains the acceleration of the center of mass of mass m_i as

$$\ddot{\mathbf{c}}_i = \ddot{s}_i\mathbf{e}_i + \mathbf{g}_i, \quad i = 1, \ldots, 4 \tag{38}$$

where

$$\mathbf{g}_i = \ddot{\mathbf{c}}_0 + \ddot{\theta}(\mathbf{E}\mathbf{c}_{i0} + s_i\mathbf{E}\mathbf{e}_i) + \dot{\theta}^2(\mathbf{E}^2\mathbf{c}_{i0} + s_i\mathbf{E}^2\mathbf{e}_i) + 2\dot{\theta}\dot{s}_i\mathbf{E}\mathbf{e}_i, \quad i = 1, \ldots, 4 \tag{39}$$

with

$$\mathbf{E} = \begin{bmatrix} 0 & -1 \\ 1 & 0 \end{bmatrix} \tag{40}$$

The force applied by the moving square frame onto the ith sliding mass is noted $\mathbf{F}_i$ while the torque applied by the square frame onto mass m_i is noted τ_i. One can then write the Newton–Euler equations applied to each of the moving masses and to the base frame as

$$\mathbf{F}_i = m_i\ddot{\mathbf{c}}_i, \quad i = 1, \ldots, 4 \tag{41}$$

$$\tau_i = I_i\ddot{\theta}, \quad i = 1, \ldots, 4 \tag{42}$$

$$\mathbf{F} - \sum_{i=1}^{4}\mathbf{F}_i = m_0\ddot{\mathbf{c}}_0 \tag{43}$$

$$\tau - \sum_{i=1}^{4}\tau_i + \sum_{i=1}^{4}((\mathbf{c}_{i0} + s_i\mathbf{e}_i)^{\mathrm{T}}\mathbf{E}\mathbf{F}_i) = I_0\ddot{\theta} \tag{44}$$

where m_0 and I_0 are the mass and inertia of the frame of the device and where $\mathbf{F}$ and τ are respectively the external force

Downloaded from ijr.sagepub.com at PENNSYLVANIA STATE UNIV on May 10, 2016

and torque applied on the frame. Substituting equations (41) and (42) into equations (43) and (44), one then obtains the relationship between the external force and torque applied on the frame of the device and the motion of the frame and of the internal masses as

$$\mathbf{F} = m_0\ddot{\mathbf{c}}_0 + \sum_{i=1}^{4}[m_i(\ddot{s}_i\mathbf{e}_i + \mathbf{g}_i)] \tag{45}$$

$$\tau = \left(I_0 + \sum_{i=1}^{4} I_i\right)\ddot{\theta} + \sum_{i=1}^{4}[m_i(\mathbf{c}_{i0} + s_i\mathbf{e}_i)^{\mathrm{T}}\,\mathbf{E}^{\mathrm{T}}(\ddot{s}_i\mathbf{e}_i + \mathbf{g}_i)] \tag{46}$$

The input accelerations of the moving masses are collected in an input acceleration vector, $\ddot{\mathbf{s}}$, defined as

$$\ddot{\mathbf{s}} = [\ddot{s}_1 \quad \ddot{s}_2 \quad \ddot{s}_3 \quad \ddot{s}_4]^{\mathrm{T}} \tag{47}$$

Equations (45) and (46) can then be rewritten in matrix form as

$$\mathbf{H}\ddot{\mathbf{s}} = \mathbf{v} \tag{48}$$

where $\mathbf{v}$ is a three-dimensional vector defined as

$$\mathbf{v} = [\mathbf{h}^{\mathrm{T}}\sigma]^{\mathrm{T}} \tag{49}$$

with

$$\mathbf{h} = \mathbf{F} - m_0\ddot{\mathbf{c}}_0 - \sum_{i=1}^{4}(m_i\mathbf{g}_i) \tag{50}$$

$$\sigma = \tau - \left(I_0 + \sum_{i=1}^{4} I_i\right)\ddot{\theta} - \sum_{i=1}^{4}[m_i(\mathbf{c}_{i0} + s_i\mathbf{e}_i)^{\mathrm{T}}\,\mathbf{E}^{\mathrm{T}}\mathbf{g}_i] \tag{51}$$

and where $\mathbf{H}$ is a 3×4 matrix which can be written as

$$\mathbf{H} = \begin{bmatrix} m_1\mathbf{e}_1 & m_2\mathbf{e}_2 & m_3\mathbf{e}_3 & m_4\mathbf{e}_4 \\ m_1(\mathbf{c}_{10}^{\mathrm{T}}\mathbf{E}^{\mathrm{T}}\mathbf{e}_1) & m_2(\mathbf{c}_{20}^{\mathrm{T}}\mathbf{E}^{\mathrm{T}}\mathbf{e}_2) & m_3(\mathbf{c}_{30}^{\mathrm{T}}\mathbf{E}^{\mathrm{T}}\mathbf{e}_3) & m_4(\mathbf{c}_{40}^{\mathrm{T}}\mathbf{E}^{\mathrm{T}}\mathbf{e}_4) \end{bmatrix} \tag{52}$$

The latter expression was simplified by noting that

$$m_i s_i \mathbf{e}_i^{\mathrm{T}}\mathbf{E}^{\mathrm{T}}\mathbf{e}_i = 0, \quad i = 1, \ldots, 4 \tag{53}$$

A generalized inverse can be used to compute the input accelerations from equation (48). For instance, the minimum-norm solution can be used to minimize the norm of the accelerations. It is pointed out that matrix $\mathbf{H}$ is always of full rank. Indeed, its columns are the planar line coordinates (direction vector and moment) of the lines associated with the four sliders. For instance, working in the moving coordinate frame attached to the frame of the device, one has

$$\mathbf{H} = \begin{bmatrix} 0 & m_2 & 0 & m_4 \\ m_1 & 0 & m_3 & 0 \\ m_1 u & m_2 u & -m_3 u & -m_4 u \end{bmatrix} \tag{54}$$

which is clearly always of full rank. In the above expression, u denotes one half of the distance between two parallel sliders. Additionally, since matrix $\mathbf{H}$ is constant in the local reference frame, its generalized inverse can be computed off-line and directly implemented in the controller.

8.2. Prescribed translational and rotational inertia

Similarly to what was done for the 1-DOF mechanism, it is desired to prescribe translational and rotational inertias for the 3-DOF inertia generator. It is noted that it is possible to prescribe a different translational inertia for orthogonal directions of motion. However, prescribing different inertias may lead to a counterintuitive behavior, depending on the application. It is assumed here that the prescribed translational inertia, noted m_a, is the same for all directions of motion. Also, the prescribed rotational inertia is noted I_a.

In the above equations, the prescribed translational and rotational inertias are used to compute the desired interaction force and moment, namely,

$$\mathbf{F} = m_a\ddot{\mathbf{c}}_0, \qquad \tau = I_a\ddot{\theta} \tag{55}$$

These equations are then substituted into equations (50) and (51), and equation (48) is then used to compute the accelerations of the moving masses that are required to produce the rendering, namely vector $\ddot{\mathbf{s}}$.

8.3. Accelerometer configuration

The above computations require the knowledge of the acceleration, angular acceleration and angular velocity of the frame of the device. These quantities can be determined using two bi-directional accelerometers mounted on the frame at points P_1 and P_2, as shown in Figure 13. Vectors $\mathbf{r}_1$ and $\mathbf{r}_2$ are respectively defined as the vectors connecting point C to points P_1 and P_2. One can then write

$$\ddot{\mathbf{p}}_i = \ddot{\mathbf{c}}_0 + \ddot{\theta}\mathbf{E}\mathbf{r}_i - \dot{\theta}^2\mathbf{r}_i, \quad i = 1, 2 \tag{56}$$

where $\ddot{\mathbf{p}}_i$ is the acceleration vector of point P_i (measured by accelerometer i). Collecting the above two equations and writing them in matrix form leads to

$$\mathbf{K}\mathbf{z} = \mathbf{m} \tag{57}$$

where $\mathbf{z}$ is the four-dimensional vector of quantities to be computed, namely

$$\mathbf{z} = [\ddot{\mathbf{c}}_0^{\mathrm{T}} \quad \ddot{\theta} \quad \dot{\theta}^2]^{\mathrm{T}} \tag{58}$$

while $\mathbf{m}$ is the four-dimensional vector of measured accelerations, i.e.

$$\mathbf{m} = [\ddot{\mathbf{p}}_1^{\mathrm{T}} \quad \ddot{\mathbf{p}}_2^{\mathrm{T}}]^{\mathrm{T}} \tag{59}$$

and matrix $\mathbf{K}$ is a 4×4 matrix that can be written as

$$\mathbf{K} = \begin{bmatrix} \mathbf{1} & \mathbf{E}\mathbf{r}_1 & -\mathbf{r}_1 \\ \mathbf{1} & \mathbf{E}\mathbf{r}_2 & -\mathbf{r}_2 \end{bmatrix} \tag{60}$$

where $\mathbf{1}$ stands for the 2×2 identity matrix. It is pointed out that if the accelerometers are placed as shown in Figure 13, matrix $\mathbf{K}$ if of full rank and can be inverted. In fact, this matrix is always invertible, as long as the two accelerometers are not located at the same point, i.e. as long as $\mathbf{r}_1 \neq \mathbf{r}_2$.

Downloaded from ijr.sagepub.com at PENNSYLVANIA STATE UNIV on May 10, 2016

Moreover, matrix **K** is constant when expressed in the local frame and it can be inverted off-line. Finally, the solution of equation (57) for **z** yields the magnitude of the angular velocity but not its sign. If the sign of the angular velocity is needed, a technique such as the one presented in Cardou and Angeles (2008) can be used.

8.4. Rendering capabilities of the 3-DOF inertia generator

The rendering capabilities of the 3-DOF inertia generator are now investigated. The ability of the mechanism to render prescribed translational inertias is assessed using a translational motion along a circular path with a constant orientation.

8.4.1. Limitations on the motion range of the moving masses As explained in Section 4, this analysis is based on harmonic motion but the results lead to design guidelines that are independent from the frequency of the input motion. A circular trajectory involving no rotation of the frame is assumed here, namely

$$x_c = r\cos(\omega t) \tag{61}$$

$$y_c = r\sin(\omega t) \tag{62}$$

$$\theta = 0 \tag{63}$$

where x_c and y_c stand for the components of vector $\mathbf{c}_0$, ω and r are respectively the frequency and the amplitude of the input motion and t is the time. Since θ is constant, one has

$$\dot{\theta} = \ddot{\theta} = 0 \tag{64}$$

Therefore, from equation (39), one can write

$$\mathbf{g}_i = \ddot{\mathbf{c}}_0, \qquad i = 1, \ldots, 4 \tag{65}$$

Differentiating equations (61) and (62) twice with respect to time, one has

$$\ddot{\mathbf{c}}_0 = -r\omega^2 \begin{bmatrix} \cos(\omega t) \\ \sin(\omega t) \end{bmatrix} \tag{66}$$

Substituting equations (55) and (65) into equation (45) then leads to

$$\sum_{i=1}^{4} (m_i \ddot{s}_i \mathbf{e}_i) = \left(m_a - m_0 - \sum_{i=1}^{4} m_i \right) \ddot{\mathbf{c}}_0 \tag{67}$$

Referring to equation (54) and working in the coordinate frame attached to the platform, the latter equation can be rewritten in component form as

$$m_2\ddot{s}_2 + m_4\ddot{s}_4 = -\left(m_a - m_0 - \sum_{i=1}^{4} m_i \right) r\omega^2 \cos(\omega t) \tag{68}$$

$$m_1\ddot{s}_1 + m_3\ddot{s}_3 = -\left(m_a - m_0 - \sum_{i=1}^{4} m_i \right) r\omega^2 \sin(\omega t) \tag{69}$$

Although it is not a necessary condition, it is now assumed that all the moving masses are equal, i.e.

$$m_i = m, \qquad i = 1, \ldots, 4 \tag{70}$$

Moreover, it is apparent that a solution of equations (68) and (69) can be obtained with

$$\ddot{s}_1 = \ddot{s}_3, \qquad \ddot{s}_2 = \ddot{s}_4 \tag{71}$$

Assuming a steady state trajectory, the latter conditions lead to

$$s_2 = s_4 = \frac{(m_a - m_0 - 4m)\, r\cos(\omega t)}{2m} \tag{72}$$

and

$$s_1 = s_3 = \frac{(m_a - m_0 - 4m)\, r\sin(\omega t)}{2m} \tag{73}$$

Referring to the last line of matrix **H** in equation (54) and substituting the above solutions into equation (46), it is readily observed that the internal mass motions of equations (72) and (73) result in $\tau = 0$, i.e. no external moment is induced, as desired. With the above solutions, masses m_2 and m_4 oscillate in phase. Masses m_1 and m_3 also oscillate in phase, with a phase difference of 90° between the two sets of masses.

The maximum range of motion of each of the four masses is assumed to be the same and is noted a, namely

$$-a \le s_i \le a, \qquad i = 1, \ldots, 4 \tag{74}$$

Therefore, substituting equations (72) and (73) into the latter equation and considering the bounds on the sine and cosine functions, one can write

$$\left(m_0 + 4m - \frac{2am}{r} \right) \le m_a \le \left(m_0 + 4m + \frac{2am}{r} \right) \tag{75}$$

The above inequalities are represented graphically in Figure 14. It is noted that the graph of Figure 14 is almost identical to that of Figure 3 except that $M = m_0 + 4m$ (total mass), the maximum value of (r/a) for which a zero virtual mass can be rendered is $2m/(m_0 + 4m)$, and the rendered to total mass ratio for $(r/a) = 1$ is bounded by $1 - 2m/M$ and $1 + 2m/M$. As a result, the maximum motion ratio (input range to actuation range) for which a zero virtual inertia can theoretically be rendered is always smaller than one half (as opposed to one for the 1-DOF device). Indeed, it can be observed that the numerator of the maximum value of r/a for which a zero virtual mass can be rendered is equal to twice the mass of one of the moving masses while there are four such masses. This result reflects the fact that the masses are mounted by pairs on orthogonal rails and that only two of the masses can be used to render inertia in a given direction (e.g. the x_0 and y_0 axes of the local frame) while the other two masses become dead weights for this direction of motion. Therefore, it can be argued that the use of four independently driven masses

Downloaded from ijr.sagepub.com at PENNSYLVANIA STATE UNIV on May 10, 2016

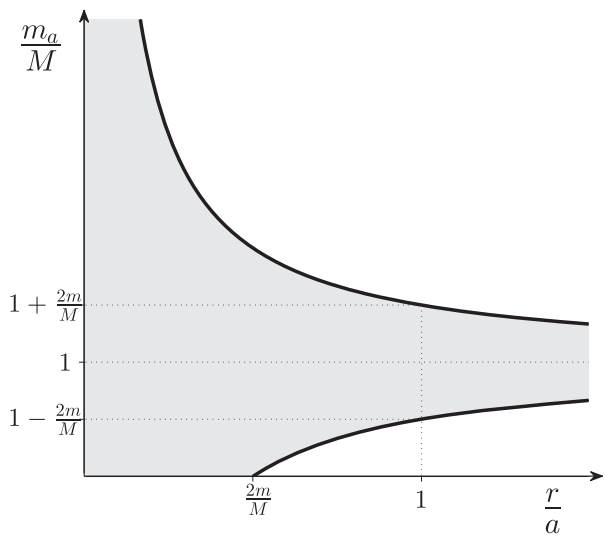

Fig. 14. Ratio of the prescribed inertia that can be rendered by the 3-DOF inertia generator to the total actual mass as a function of the ratio of the input motion range to the moving masses motion range. The shaded area represents the feasible region.

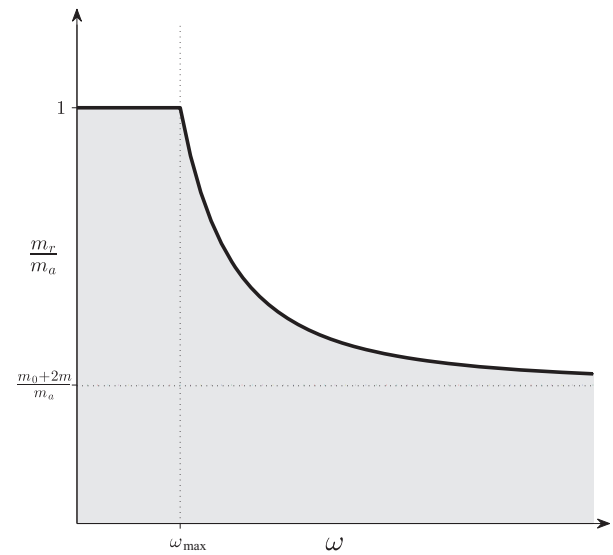

Fig. 15. Ratio of the rendered inertia over the prescribed inertia as a function of the frequency of the input motion considering the acceleration limit of the actuators of the 3-DOF inertia generator.

is not optimal from the point of view of inertia generation. Indeed, the use of a single larger mass mounted on a 3-DOF mechanism may seem more efficient. However, such an arrangement is more complex and may also lead to inefficient inertias because the links of the 3-DOF mechanism also introduce spurious inertias. Moreover, in order to be able to generate significant rotational inertial effects with a single rigid body, the latter should have a relatively large radius of gyration, which would significantly increase its size and therefore reduce the allowable motion range. From the above derivations, it is clear that a reduced motion range is highly detrimental to the rendering capabilities of an inertia generator. Hence, it is believed that the architecture proposed here is a reasonable compromise between complexity and effectiveness.

8.4.2. Limitations on the actuator velocities and accelerations Similarly to what was done in the case of the 1-DOF device, the performance limitations introduced by the limited feasible velocities and accelerations of the actuators should also be assessed. The acceleration limits correspond to the limits on the absolute acceleration of the moving masses with respect to a fixed inertial frame. For the translational trajectory defined in equations (61) and (62), the acceleration limits are applied on $(\ddot{x}_c + \ddot{s}_i)$ and $(\ddot{y}_c + \ddot{s}_i)$. Each of the components of equation (67) then leads to an equivalent equation that can be written as

$$2m_i\ddot{s}_2 = 2m\ddot{s}_i = (m_a - m_0 - 4m)\ddot{x}_c \tag{76}$$

If the maximum force that can be applied by one of the actuators is noted $F_{i,\max}$, the corresponding maximum frequency of the trajectory defined in equations (61) and (62) can be obtained by writing

$$F_{i,\max} = m(\ddot{x}_c + \ddot{s}_2) \tag{77}$$

in which equation (76) and the second derivative of equation (61) are substituted. After a few simple manipulations, one obtains

$$\omega_{\max}^2 = \frac{2F_{i,\max}}{r|m_a - m_0 - 2m|} \tag{78}$$

Equation (78) provides the maximum frequency for which the prescribed translational inertia m_a can be rendered. For frequencies above $\omega_{\max}$, the analysis presented in Section 4.2 is repeated here for the 3-DOF mechanism using the translational circular trajectory defined above, which leads to

$$\frac{m_r}{m_a} = \frac{m_0 + 2m}{m_a} + \left(1 - \frac{(m_0 + 2m)}{m_a}\right)\frac{\omega_{\max}^2}{\omega^2} \tag{79}$$

The resulting behavior is illustrated in Figure 15. Similarly to what was observed for the 1-DOF mechanism, the rendered inertia is equal to the prescribed inertia when $\omega \leq \omega_{\max}$ while the rendered inertia differs from the prescribed inertia for higher frequencies. For very high frequencies, the rendered inertia converges to $(m_0 + 2m)/m_a$. The term $2m$ appearing in the numerator of this ratio arises from the fact that the masses are mounted on orthogonal rails and that for any direction of motion, half of the masses act as dead weights.

The effect of velocity limitations is similar to what was observed for the 1-DOF device and the derivation is similar

Downloaded from ijr.sagepub.com at PENNSYLVANIA STATE UNIV on May 10, 2016

to that of Section 4.2. Considering equations (68) and (69), assuming the steady state trajectory defined in equations (61) and (62) and four equal masses, one can write

$$2m\dot{s}_i = (m_a - m_0 - 4m)\dot{x}_c = -(m_a - m_0 - 4m)r\omega\sin(\omega t) \tag{80}$$

which leads to

$$\omega'_{\max} = \frac{2m\dot{s}_{i,\max}}{r|m_a - m_0 - 4m|} \tag{81}$$

where $\omega'_{\max}$ is the maximum frequency for which the prescribed inertia can be rendered considering the velocity limitations of the actuators. For input frequencies larger than $\omega'_{\max}$, the maximum velocity of the actuators is reached and hence the acceleration $\ddot{s}_i$ is zero over a certain phase of the motion. Considering the trajectory defined in equations (61) and (62) and assuming $\ddot{s}_i = 0$, equations (48), (50), and (39) lead to

$$F_x = (m_0 + 4m)\ddot{x}_c \tag{82}$$

which means that the rendered inertia over this phase of the motion is equal to $(m_0 + 4m)$, i.e. the actual total mass of the device. This is equivalent to what was observed for the 1-DOF device. As explained in Section 4, the effect of this limitation may not be as drastic as it appears because the degradated rendering takes place in a phase of the motion during which the acceleration is low. Nevertheless, both acceleration and velocity limitations should be taken into account in a practical design.

8.5. Simulation results

Simulations were conducted in order to further investigate the capabilities of the 3-DOF inertia generator described above. Examples of simulation trajectories are now provided in order to illustrate the results.

8.5.1. Translational motion First, the results obtained with a translational trajectory are reported. The trajectory consists of a lemniscate, which can be described in parametric form as

$$x_c = \frac{b\sqrt{2}\cos\beta}{1+\sin^2\beta}, \quad y_c = \frac{b\sqrt{2}\sin\beta\cos\beta}{1+\sin^2\beta}, \quad \beta = \omega t \tag{83}$$

where b is a scaling factor, ω is the frequency with which the trajectory is performed ($\omega = \pi/2$ here) and t is the time. The trajectory used in the simulation ($b = 0.07m$) is represented graphically in Figure 16.

The center of the frame of the inertia generator follows the trajectory defined by the lemniscate while the orientation remains unchanged ($\theta = \dot{\theta} = \ddot{\theta} = 0$). The masses are initially at rest and located at the mid-point of their moving range. The prescribed translational inertia is equal to 75% of the total mass of the device, i.e. $m_a/M = 0.75$. Also, the amplitude of motion (distance from the origin of the fixed frame to the extreme points of the lemniscate is equal to approximately 40% of the amplitude of motion allowed for the masses, namely $r/a \simeq 0.4$. Finally, each of the moving masses has a mass equal to approximately 114% of the mass of the frame, which leads to a ratio of $2m/(m_0 + 4m) \simeq 0.4$. It is recalled that this ratio is defined in the preceding section as a design guideline for low inertia rendering. Hence, according to the analysis presented in the preceding section, the amplitude of the trajectory prescribed in this simulation and the prescribed inertia selected should be within the capabilities of the inertia generator, which is readily observed on the graphs provided below.

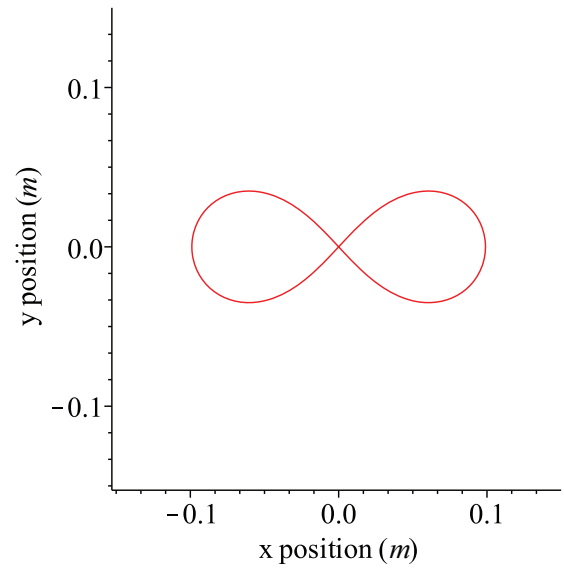

Fig. 16. Translational trajectory consisting of a lemniscate with $b = 0.07m$.

The results of the simulation are shown in Figure 17. Figure 17(a) shows the force components rendered to the user. These force components correspond exactly to the inertial effects associated with the prescribed virtual inertia. In other words, the generator is capable of rendering the prescribed inertia at all times. In order to render these inertial forces, the masses undergo the displacements shown in Figure 17(b). It can be observed that, after having completed one full cycle of the lemniscate, the masses have drifted away from their mid-range initial position. This situation arises from the fact that the initial conditions on the masses (initial position and velocity) do not match the steady state conditions of the lemniscate. These results highlight the importance of using a washout filter in a practical implementation (no washout filter was used in the simulation). Figure 17(c) confirms that no moment is generated in the simulation, i.e. the motion of the masses is such that the moments generated by the individual masses (see Figure 17(d)) always cancel out exactly, as enforced by equation (48).

Downloaded from ijr.sagepub.com at PENNSYLVANIA STATE UNIV on May 10, 2016

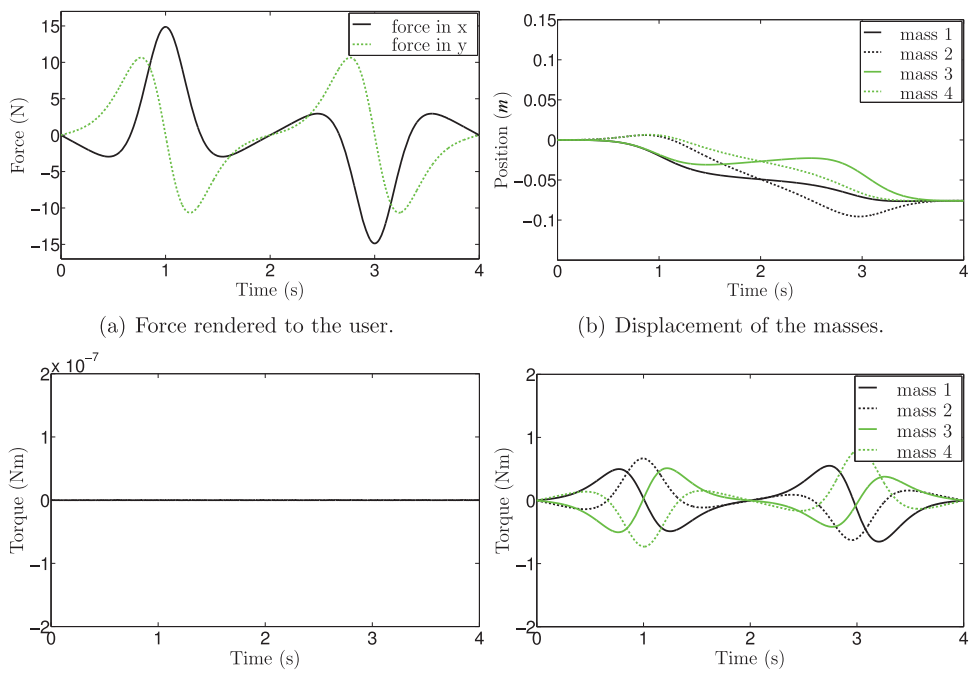

(a) Force rendered to the user. (b) Displacement of the masses.

(c) Torque rendered to the user. (d) Torque induced by the masses.

Fig. 17. Simulation of the planar 3-DOF inertia generator performing a translational trajectory consisting of a lemniscate ($b = 0.07$, $\omega = \pi/2$).

8.5.2. Rotational motion In this simulation, a rotational motion of the inertia generator with respect to its centroid is prescribed. The trajectory is described as

$$x_c = 0, \qquad y_c = 0, \qquad \theta = \eta \sin(\omega t) \tag{84}$$

where η is a scaling factor, ω is the frequency at which the trajectory is performed ($\omega = \pi$ here) and t is the time. The trajectory used in the simulation uses a range of rotation of $\eta = \pi/6$, and the prescribed rotational inertia is equal to 85% of the total inertia of the generator.

The results of the simulation are shown in Figure 18. Figure 18(a) shows that the force rendered to the user is identically equal to zero, as expected. The contribution of each of the masses to the rendered forces is shown in Figures 18(c) and (d), where it can be observed that the effect of the masses cancels out. The displacement of the masses, which is required in order to render the prescribed inertia, is shown in Figure 18(b). Referring to Figure 13, it can be observed that the masses are 'rotating' around the center of the generator in order to produce a counter inertia that reduces the actual inertia thereby rendering the prescribed inertia. It can also be observed that the masses are drifting away from their initial position after one cycle of oscillation has been performed, which is is due to the initial conditions that do not correspond to the steady state of the oscillating trajectory. Such a drift can be alleviated using a washout filter. The contribution of each of the masses to the counter inertia is the same, due to the symmetry of the device. This can be observed in Figure 18(f) where the contribution of each of the masses to the rendered rotational inertia is plotted. Finally, Figure 18(e) shows that the correct inertia is rendered.

9. Conclusion

The concept of inertia generator is proposed in this paper. In an inertia generator, internal masses are moved in reaction to accelerations induced by the user such that the effective intertia of the device is modified in order to render a prescribed (programmable) inertia. This paper presented preliminary investigations on a 1-DOF inertia generator that has the capability to render a translational inertia in one direction. The dynamic model of the system was first derived. Based on this model, the rendering capabilities of the inertia generator were investigated and general guidelines were proposed for its design. The range of input frequencies that can be properly rendered was also determined based on the acceleration and velocity limitations of the actuator. A controller that uses the measured acceleration of the frame as an input and determines the motion of the internal mass as an output was then developed. The controller is based on the time integration of the acceleration in order to alleviate the difficulties associated with noisy accelerometer signals. A velocity or position control can therefore be used. Experimental results show that, although the power to mass ratio and the moving mass to frame mass ratio of the prototype are not high, the latter is capable of rendering a significant range of inertias. Moreover, experimental

Downloaded from ijr.sagepub.com at PENNSYLVANIA STATE UNIV on May 10, 2016

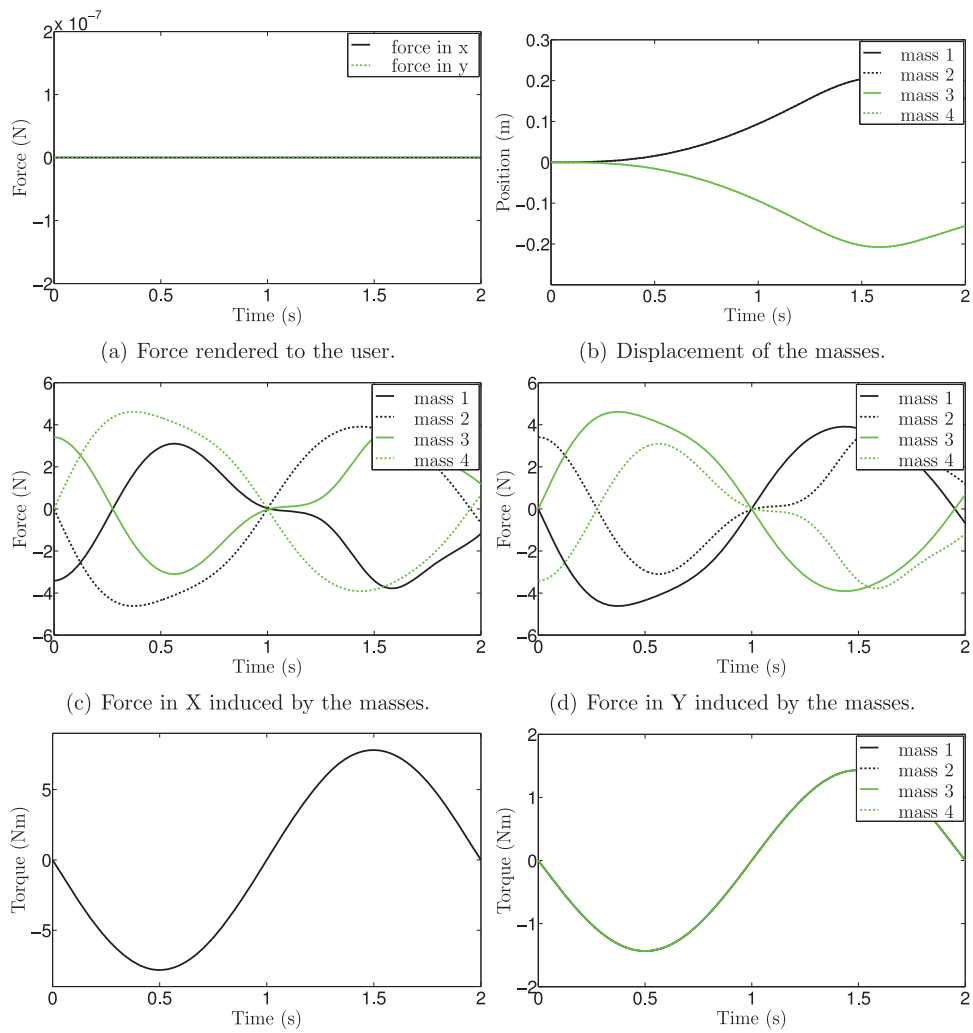

(a) Force rendered to the user.

(b) Displacement of the masses.

(c) Force in X induced by the masses.

(d) Force in Y induced by the masses.

(e) Torque rendered to the user.

(f) Torque induced by the masses.

Fig. 18. Simulation of the planar 3-DOF inertia generator performing a pure rotation ($\eta = \pi/6$, $\omega = \pi$).

data was shown to concur with the rendering capabilities predicted by the theoretical analyses.

The concept was then extended to a planar 3-DOF inertia generator capable of rendering translational inertia in two directions as well as rotational inertia. The proposed architecture consists of four masses mounted on orthogonal rails attached to the frame of the inertia generator. Two bi-directional accelerometers are used to compute the acceleration, angular velocity and angular acceleration of the frame. Based on these measurements and on the prescribed inertias, the required motion of the moving masses is computed using a robust dynamic model. It was shown that the matrix computations required are stable and that the inversions can be computed off-line. An analysis of the rendering capabilities of the 3-DOF generator was conducted, which led to general design guidelines. The range of input frequencies that can be rendered was also investigated based on the acceleration and velocity limitations of the actuators. Example simulations were provided and the results demonstrated the feasibility of the 3-DOF inertia generator. A prototype of a 3-DOF inertia generator is currently being designed and built. Future work includes the experimental validation of the 3-DOF prototype, the investigation of spatial multi-DOF inertia generators and the experimentation with more advanced prototypes.

Acknowledgement

The authors would like to thank Mr. Frédéric Lessard for his help with the design of the 1-DOF prototype.

Funding

This work was supported by the Natural Sciences and Engineering Research Council of Canada (NSERC) (grant number 89715), by the Canada Research Chair program (grant number 203732), and by the Fonds de Recherche du Québec – Nature et Technologie (FRQ-NT) (grant number PR-175006).

Downloaded from ijr.sagepub.com at PENNSYLVANIA STATE UNIV on May 10, 2016

References

Amemiya T, Ando H and Maeda T (2008) Lead-me interface for a pulling sensation from hand-held devices. *ACM Transactions on Applied Perception* 5(3): no. 15.

Ando H, Sugimoto M and Maeda T (2004) Wearable moment display device for nonverbal communication. *IEICE Transactions on Information and Systems* E87-D(6): 1354–1360.

Armstrong-Helouvry B, Dupont P and Canudas De Wit C (1994) A survey of models, analysis tools and compensation methods for the control of machines with friction. *Automatica* 30(7): 1083–1138.

Cardou P and Angeles J (2008) Estimating the angular velocity of a rigid body moving in the plane from tangential and centripetal acceleration measurements. *Multibody System Dynamics* 19(4): 383–406.

Ebert-Uphoff I and Dang A (2004) Active acceleration compensation for transport vehicles carrying delicate objects. *IEEE Transactions on Robotics* 20(5): 830–839.

Graf R and Dillmann R (1997) Active acceleration compensation using a Stewart platform on a mobile robot. In: *Proceedings of 2nd EUROMICRO workshop on advanced mobile robots*, Brescia, Italy, 22–24 October, pp.59–64.

Hannaford B and Okamura A (2008) Haptics. In: Siciliano B and Khatib O (eds) *The Springer Handbook of Robotics*. Berlin: Springer, pp.719–739.

Hassouneh M, Lee H and Abed E (2004) Washout filters in feedback control: Benefits, limitations and extensions. In: *Proceedings of the 2004 American control conference*, Boston, MA, 30 June–2 July 2004, Vol. 5, pp.3950–3955.

Laitinen P and Maenpaa J (2006) Enabling mobile haptic design: Piezoelectric actuator technology properties in handheld devices. In: *IEEE international workshop on haptic audio visual environments and their applications*, Ottowa, ON, 4–5 November 2006, pp.40–43. doi: 10.1109/HAVE.2006.283787.

Lecours A, Mayer-St-Onge B and Gosselin C (2012) Variable admittance control of a four-degree-of-freedom intelligent assist device. In: *IEEE International conference on robotics and automation*. Saint Paul, MN, 14–18 May 2012, pp.3903–3908.

Moen J (2007) From hand-held to body-worn: Embodied experiences of the design and use of a wearable movement-based interaction concept. In: *First International conference on tangible and embedded interaction*, Baton Rouge, LA, 15–17 February 2007, pp.251–258.

Nahon M and Reid L (1990) Simulator motion-drive algorithms, a designer's perspective. *Journal of Guidance, Control and Dynamics* 13(2): 356–362.

Nakamura N and Fukui Y (2006) Development of a force and torque hybrid display "GyroCubeStick". In: *First joint Eurohaptics conference, 2005, and symposium on haptic interfaces for virtual environment and teleoperator systems, 2005 (World haptics 2005)*, Pisa, Italy, 18–20 March 2005, pp. 633–634.

Wever J, Gosselin C and Herder J (2013) On the design of a portable force illusion device for navigation aids. In: *ASME International design engineering technical conferences*, Portland, OR, 4–7 August 2013, DETC2013-12374.

Winfree K, Gewirtz J, Mather T, Fiene J and Kuchenbecker K (2009) A high fidelity ungrounded torque feedback device: The iTorqU 2.0. In: *Third joint Eurohaptics conference and symposium on haptic interfaces for virtual environment and teleoperation systems*, Salt Lake City, UT, 18–20 March 2009, pp. 261–266.

Appendix: Index to Multimedia Extensions

The multimedia extension page is found at http://www.ijrr.org.

Table of Multimedia Extensions

Extension	Type	Description
1	Video	A video demonstrating the operation of the prototype of the 1-DOF inertia generator.

Downloaded from ijr.sagepub.com at PENNSYLVANIA STATE UNIV on May 10, 2016